Direct imaging of the alternating disordered and crystalline structure of cellulose fibrils via super-resolution fluorescence microscopy

Mouhanad Babi,[1] Anthony Palermo,[1] Tiffany Abitbol,[2] Ayodele Fatona,[1], Victoria Jarvis,[3] Akanksha Nayak,[1] Emily D. Cranston,[2,4,5] and Jose M. Moran-Mirabal[1,6]*

[1]*Department of Chemistry and Chemical Biology, McMaster University, Hamilton, ON, L8S 4M1, Canada*

[2]*RISE Research Institutes of Sweden, Stockholm, Sweden*

[3]*McMaster Analytical X-ray Diffraction Facility, McMaster University, Hamilton, ON, L8S 4M1, Canada*

[4]*Department of Wood Science, University of British Columbia, 2424 Main Mall, Vancouver, BC, V6T 1Z4, Canada*

[5]*Department of Chemical and Biological Engineering, University of British Columbia, 2360 East Mall, Vancouver, BC V6T 1Z3, Canada*

[6]*Centre for Advanced Light Microscopy, McMaster University, Hamilton, ON, Canada*

[7]*Brockhouse Institute for Materials Research, McMaster University, Hamilton, ON, Canada*

*Correspondence to: mirabj@mcmaster.ca

ABSTRACT

Cellulose, the primary component of the plant cell wall, has fueled the wood, textile, pulp and paper industries for centuries, and has recently been used for the production of renewable nanomaterials. The tight crystalline packing of glucan chains within cellulose fibrils is responsible for its superior mechanical properties but renders this material recalcitrant to biochemical and chemical breakdown and limits its use as a green resource. The presence of nanoscale dislocations within cellulose fibrils has been postulated for decades and is thought to be responsible for the production and size of cellulose nanocrystals (CNCs) following acid hydrolysis. However, dislocations have never been directly visualized and their prevalence and size have remained elusive. In this study, we have used super-resolution (SR) fluorescence microscopy to directly visualize and measure alternating crystalline and disordered regions within individual fluorescently labelled bacterial cellulose fibrils. The measured size of the crystalline regions ranges from 40 – 400 nm and shows striking overlap with the length distribution of bacterial CNCs produced through sulfuric acid hydrolysis, supporting the fringed micellar model for the supramolecular structure of cellulose fibrils. The disordered regions were found to be 20 – 120 nm in length and show heterogeneous accessibility, which directs fibril cleavage during the initial stages of cellulose acid hydrolysis. Two-colour SR imaging of cellulose fibrils and bound exoglucanases (Cel7A), in combination with degree of crystallinity measurements suggest that these dislocations are nanoscale in size, and do not result in amorphous cellulose pockets large enough to accommodate enhanced enzyme binding. Through characterization of disordered regions in cellulose fibrils, we have gained insight into the role of cellulose nanostructure in its breakdown by chemical and enzymatic means.

INTRODUCTION

Cellulose is a structural polysaccharide that is naturally produced by plants and other organisms at an annual rate of over a 100 billion tonnes, making it the most abundant biopolymer on Earth.[1,2] The compact assembly of cellulose chains into fibrils, bundles and higher order structures is directly linked to its biosynthesis and provides plants with the necessary strength and protection to survive, while endowing wood with the mechanical strength that makes it an attractive building material.[3] Recently, the deconstruction of cellulose through mechanical and chemical processes has resulted in the production of cellulose nanofibrils and nanocrystals for applications in nanomedicine, biodegradable composite materials, and biosensing, among others.[4,5] At the same time, cellulose can be completely broken down into soluble sugars and fermented to produce biofuels, allowing us to exploit the sunlight captured by plants through photosynthesis as a renewable source of energy. However, the conversion of cellulose to nanomaterials and soluble sugars is currently inefficient due to its crystalline structure that renders it recalcitrant to depolymerization.[6] Thus, it is important to study the supramolecular structure of cellulose at the nanoscale to understand its function within plants and other organisms, and to develop more efficient methods for processing it.[7]

At the molecular level, a cellulose polymer chain is composed of 1,000 to 20,000 anhydroglucose units that are linearly connected through β-1→4 glycosidic linkages.[4,8] During cellulose biosynthesis, intermolecular hydrogen bonds and van der Waals forces assemble 18-36 chains into a tightly packed, crystalline cellulose microfibril that is 2 to 4 nm wide.[9–11] Plant-derived cellulose fibrils contain a sheath of lignin and hemicellulose that assist in assembling them into bundles, macrofibrils and higher-order networks that form the scaffold of the plant cell wall.[12,13] The covalent and intermolecular bonds involved in the crystalline packing of cellulose endow it with its exceptional mechanical strength and a Young's modulus (>100 GPa) that is comparable to that of steel or Kevlar.[14,15] However, this organization also renders most of the glucan chains inaccessible to chemical reagents and enzymes, making it challenging to efficiently break cellulose down to produce nanomaterials and biofuels.

It has been postulated for over seven decades that cellulose fibrils possess regularly occurring disordered regions that are easily cleaved during acid hydrolysis to produce cellulose nanocrystals (CNCs).[4,16] These needle-like particles are 100 – 300 nm in length and become progressively shorter as they are hydrolyzed for longer periods of time.[17] Interestingly, after a short period of hydrolysis, the degree of polymerization of CNCs levels-off (LODP).[17,18] The non-linear depolymerization kinetics of cellulose suggested that the crystalline structure of the fibril is interspersed with periodic disordered regions that are significantly more accessible to small molecules and therefore more susceptible to hydrolysis.[17] This alternating crystalline and disordered supramolecular structure of cellulose fibrils has been referred to as the "fringed micellar model", where highly crystalline cellulose micelles are connected through more loose, fringed cellulose material.[8,19]

While the fringed-micellar model of cellulose fibrils is often used to explain the production of CNCs,[4,20,21] it has been supported only by a few studies that characterize the supramolecular structure of cellulose. Through small-angle neutron scattering (SANS), Nishiyama and colleagues detected regularly occurring disordered regions that exhibited enhanced accessibility to deuterated water compared to the crystalline portion of ramie cellulose fibrils.[22] The disordered regions possessed a periodicity of 150 nm, which corresponded well to the LODP of acid hydrolyzed fibers

and supported the alternating crystalline and disordered structure of cellulose. However, the origin of these dislocations and whether they occur naturally has been a source of debate, as kinks and nanoscale defects that show enhanced susceptibility to hydrolysis can be induced through mechanical stresses.[23,24] On the other hand, observations made through SANS, solid-state NMR, Fourier transform infrared spectroscopy and atomic force microscopy have resulted in the proposal of an alternative core-shell model, where the disordered fraction of cellulose lies on the surface of the fibril.[9,25,26] Due to little direct evidence, the natural organization of native cellulose fibrils in a fringed-micellar or core-shell structure has been controversial over the past decades.[9,10,26] If the fringed-micellar model is correct, then the prevalence, size, morphology, origin and biological role of the disordered regions and how they drive cellulose hydrolysis remains to be understood. Moreover, whether the disordered regions are truly amorphous and their contribution to the overall crystallinity index of cellulose remains unclear, as wide-angle X-ray diffraction (XRD) measurements are highly impacted by the presence of impurities, mode of data collection, and the fitting methods used to analyze the diffractograms.[27]

We hypothesized that the obstacles in visualizing nanoscale dislocations could be overcome by high resolution fluorescence microscopy, as the process of labeling cellulose with small organic dyes could probe the accessibility of different regions along the cellulose fibril. Until recently, the resolution of conventional fluorescence microscopy was limited by the diffraction of light to ~200 nm, which prevented its use to study labeling patterns at the nanoscale. The development of super-resolution approaches over the last decades has revolutionized the field of fluorescence microscopy and has allowed imaging with resolutions that surpass the diffraction limitations. A subset of these super-resolution techniques exploit the photo-blinking behaviour of fluorophores to temporally deconvolve their emission and subsequently localize them with nanometer precision, resulting in reconstructed images with typical resolutions of 20 – 40 nm.[28,29] In addition to visualizing the nanoscale morphology of fibrils, super-resolution imaging can provide quantitative information on the relative or absolute amounts of molecules present in any given region.[30] This would allow us to assess local variations in fluorescence labeling and draw conclusions on the susceptibility of the underlying structures to chemical modification. Overall, these developments have provided new tools to study cellulose structure at the nanoscale and open the door to the visualization of dislocations in the crystalline arrangement of cellulose fibrils.

In this work, we used stochastic optical reconstruction microscopy (STORM) to directly visualize nanoscale disordered regions within highly crystalline bacterial cellulose fibrils extracted from *Komagataeibacter xylinum*. Bacterial cellulose (BC) is a suitable crystalline cellulose model as it does not contain lignin and hemicellulose and thus can be extracted in its native form through mild treatments. Following the grafting of small organic fluorescent dyes, the disordered and crystalline regions of the fibrils were visualized using STORM and characterized for their size, dispersity, and relative degrees of accessibility (**Figure 1**, top). Additionally, temporally controlled sulfuric acid hydrolysis of BC fibrils was used to produce bacterial CNCs, which allowed us to compare the prevalence of nanoscale dislocations visualized through STORM with the length of the CNCs, providing insight into their mechanism of production (**Figure 1**, bottom). Our results strongly support the fringed-micellar model of cellulose fibril structure and highlight the prevalence and heterogeneity of the disordered regions within BC fibrils (**Figure 1**, middle). We propose that this visualization technique can be further extended to directly characterize the nanoscale structure of cellulose fibrils derived from other sources. The accurate characterization of nanoscale dislocations is key to our understanding of the structure-function relationship of

cellulose in an industrial and biological context, and critical to the development of more efficient methods for the breakdown of this natural resource to produce renewable nanomaterials, biofuels, bioplastics and other sustainable consumer products.

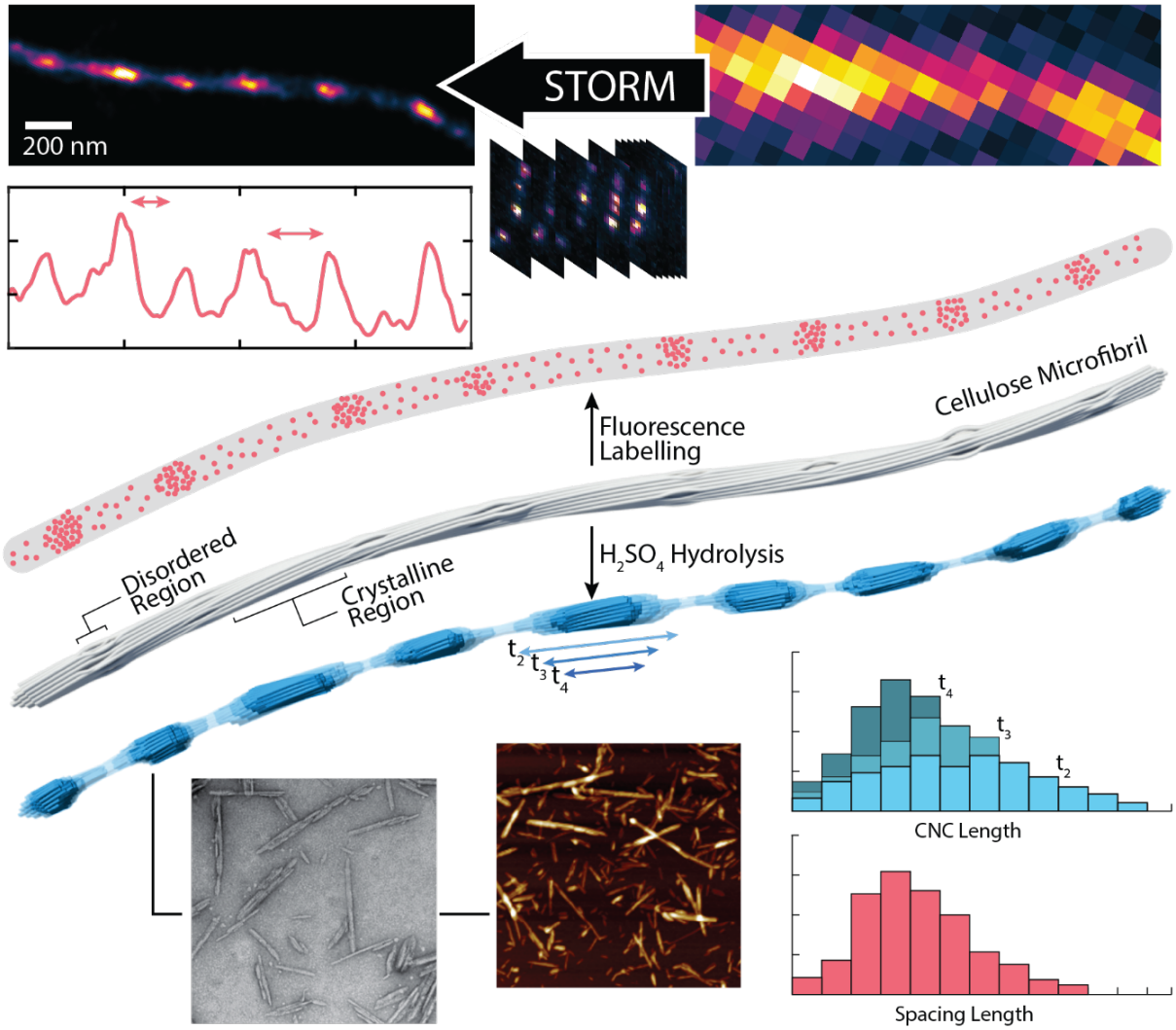

Figure 1. Super-resolution fluorescence imaging allows the direct visualization of disordered regions in bacterial cellulose fibrils. The fringed-micellar model of the ultrastructure of cellulose (middle, grey) proposes the existence of alternating disordered and ordered regions along cellulose fibrils. Disordered regions would be more accessible than highly crystalline ones, making them more susceptible to labeling with dyes (top, red) or degradation (bottom, blue). In this model, the disordered regions are preferentially hydrolyzed, and the cellulose fibril is eventually segmented at these regions, leaving behind cellulose nanocrystals (CNCs). CNC dimensions can be measured for different extents of acid hydrolysis (t_1, t_2…t_4). Fluorescence labeling would result in fluorophore clusters at the more accessible (i.e., disordered) regions. The resolution offered by STORM unveils a pattern of alternating bright and dark areas corresponding to disordered and crystalline regions. The size of the crystalline regions and their distribution (red histogram) would correspond to that of CNCs (blue histogram). To clearly show the dislocations, the fibril is represented with a significantly lower length to width ratio than in real cellulose fibrils.

RESULTS & DISCUSSION

BC produced by *Komagataeibacter xylinum* (formerly known as *Acetobacter xylinum* and *Gluconacetobacter xylinus*)[31] was purified from the foodstuff *nata de coco* through mild alkaline treatment, producing micrometer-long cellulose ribbons (**Figure 2a**) with an average width of 40 ± 20 nm, as measured by TEM (n > 100 fibrils). AFM imaging revealed that the bacterial cellulose ribbons have non-uniform cross-sections in the 10 – 50 nm range (**Figure 2b**), with frayed ends showing fibrils with diameters below 10 nm. The length, width and height observations agree with previous characterization of BC purified from *nata de coco* and *K. xylinum* cultures.[32,33] We also observed twists and striations along the longitudinal axis of the cellulose ribbons with widths of ~10 nm in both AFM and TEM images, consistent with previous observations of pure BC.[32] The morphology and texture of the purified BC samples suggest that the ribbons contain 12 nm-wide bundles of cellulose microfibrils, and that the samples isolated form *nata de coco* are free from sugar and protein impurities that are found in the original foodstuff. Due to inconsistencies in the terminology used in the literature to describe the different hierarchical levels of bacterial cellulose ribbons,[32,34] and to remain consistent with what is typically used to describe plant cellulose,[13] the term "fibril" will be used to represent thin ribbons that consist of 1 – 3 microfibril bundles.

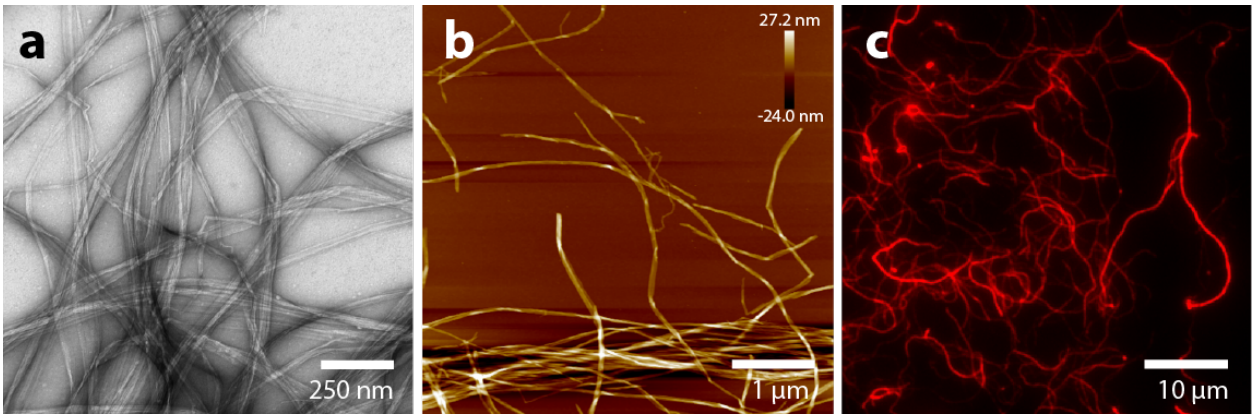

Figure 2. Images of purified bacterial cellulose. (a) Transmission electron microscopy image of BC showing the striations within fibrils and their tendency to twist. **(b)** Atomic force microscopy of cellulose showing BC fibrils. (**c**) Fluorescent BC imaged using epifluorescence microscopy, showing loosely bound meshes of cellulose fibrils. Fibrils appear larger in epifluorescence due to the limitations in resolution imposed by the diffraction of light.

To study the nanostructure of cellulose fibrils using STORM, BC was fluorescently labelled with organic dyes using two approaches based on triazinyl linkers. Triazine chemistry has been widely used to covalently link dyes and pigments onto the abundant primary hydroxyl groups present in cellulose. This chemistry provides the advantage of aqueous reactions under mild conditions, which ensures that the BC nanostructure and crystallinity remain unchanged.[35–37] In the first labeling approach, the commercially-available dichlorotriazinyl aminofluorescein (DTAF) and the in-house synthesized dichlorotriazinyl piperazine-rhodamine 6G (DTPR) were directly grafted onto cellulose (**Figure S1a**) using previously reported protocols.[36,38,39] A second labeling strategy was also used where BC was first functionalized with dichlorotriazinyl propargylamine (DTAP), which could then undergo click reaction with azide-bearing molecules. This enabled us to label cellulose with a higher density and a variety of commercially available

dyes that possess an azide chemical handle, such as 6-carboxyfluorescein azide (FAM) and cyanine 5 azide (Cy5) (**Figure S1b**).

Fluorescently labelled BC displayed a range of hierarchical structures with lengths in the tens to hundreds of micrometers and widths that spanned from submicrometer-wide large, bright ribbons to dim fibrils with widths below the diffraction-limited resolution of the optical microscope (~200 nm). In agreement with TEM and AFM observations (**Figures 2a-b**), these fibrils were usually entangled and formed loose meshes (**Figure 2c**). Occasionally, isolated cellulose fibrils were found, which exhibited a variety of curved configurations due to their inherent flexibility.[26,40] With epifluorescence microscopy, the diffraction-limited fibrils appeared uniformly labelled along their length. In contrast, imaging with STORM unveiled a consistent pattern of alternating dark and bright regions along the length of the fibrils (**Figure 3a**), while resolving features smaller than 40 nm (**Figure 3b** (inset) and **Figure 3d**).

The one-dimensional pattern was observed on fibrils labelled directly with DTAF or DTPR dyes, as well as on those labeled first with an alkyne-triazinyl derivative followed by a click reaction with FAM or Cy5 dyes. In the case of Cy5-BC, the fibrils were continuously mapped along their length with a high density of fluorophore localizations and exhibited a similar labeling pattern when the concentration of dye used in the labeling reaction was doubled (**Figure S2** and **Figure S3**). These observations indicate that the pattern was not an imaging artifact or a result of inadequate labeling and sampling, as it was independent of the type of dye, label concentration and labeling reaction used. Instead, it implies that the labeling pattern is a result of features encoded within the nanostructure of the cellulose fibrils. The presence of highly contrasted dark and bright regions along the fibril reflects regions with different density of the linked fluorophores, suggesting that some areas of the fibril are more accessible and susceptible to covalent modification than others. We thus hypothesized that the dark regions of the fibril (less accessible to labeling, yielding fewer localizations) represent crystalline cellulose, while brighter regions (more accessible to labeling, yielding more localizations) represent dislocations or areas where glucan chains are less ordered.

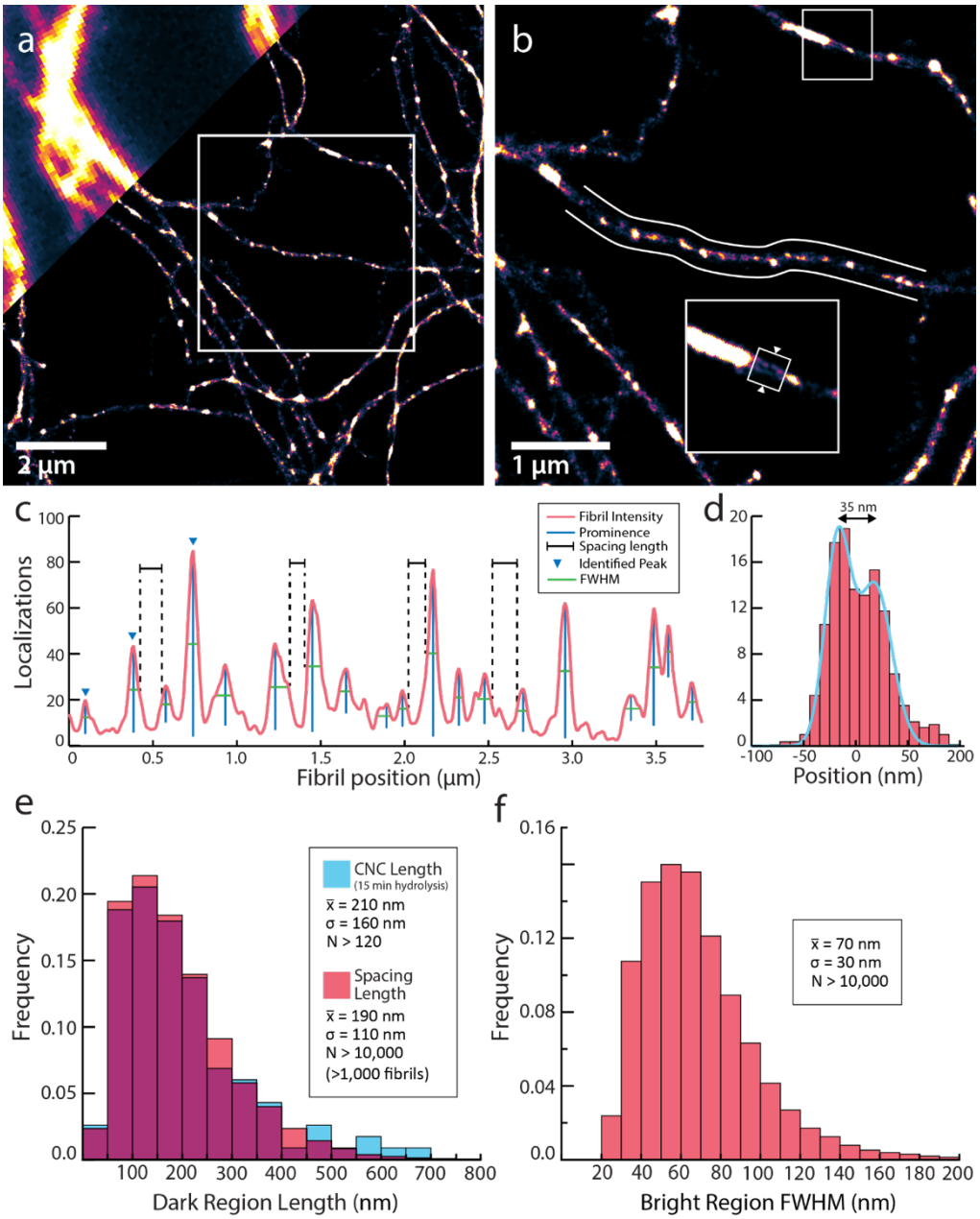

Figure 3. Quantitative analysis of the labeling pattern observed in Cy5-BC fibrils. (a) STORM super-resolution images of Cy5-BC fibrils revealed a pattern of alternating dark and bright regions throughout the length of the fibrils. **(b)** This pattern was analyzed by tracing the dimmest cellulose fibrils (representing the thinnest bundles) and generating intensity profiles along the longitudinal axis. **(c)** Bright peaks were identified within the profile and their full width at half maximum (FWHM) and maximum intensity were measured. **(d)** Sub-50 nm features, such as the fibril twisting shown in the inset of panel b, were occasionally seen in super-resolution images **(e)** The length of the dark regions was calculated as the distance between adjacent peaks at half their maximum intensity. Their distribution (red) matches the length (measured by TEM) for CNCs produced by 15 minutes of acid hydrolysis (teal) with the overlap shown in purple. **(f)** In comparison, the distribution of the size of the bright regions (FWHM of the peaks) were significantly smaller.

The size of the putative crystalline (dark) and disordered (bright) regions was quantified by tracing the dimmest individual fibrils (representing the thinnest microfibril bundles, **Figure 3b**) and acquiring line-intensity profiles (**Figure 3c**). The profiles of labeled fibrils exhibited many sharp, well-separated peaks with heterogeneous intensities and separation distances (**Figure 3c**). A semi-logarithmic histogram of the aggregated intensity values for pixels along the fibril profiles displayed a bimodal distribution (**Figure S3**, bottom) for fibrils labeled with either DTAF or Cy5. For DTAF-BC, the first population was representative of the sparse labeling found in the dark regions, while the second population presented intensities 10 to 100-fold brighter, consistent with the densely labeled bright regions. The leftmost population was considerably less prominent in Cy5-BC and almost completely disappeared when the dye concentration was doubled. This indicates that the dark regions in DTAF-BC were completely devoid of localizations and possessed an intensity similar to that of the image background, while Cy5-BC exhibited labeling throughout the fibrils. These differences are attributed to the higher labeling densities permitted by the two-step labeling method and superior photophysical properties of Cy5, including the ability to reactivate it using UV light, in addition to having higher photostability, photoswitching rate, and brightness.[41] These properties result in a higher dynamic range for the comparison of the intensities between the crystalline and disordered regions. With this in mind, Cy5-BC was selected for further analysis and characterization of the labeling patterns observed in the fibrils.

The brightly labeled peaks representative of the disordered cellulose regions were systematically identified using a median prominence threshold based on all the local maxima present in a given intensity profile (**Figure S2**). The size of the dislocations was then measured by determining the full width at half maximum (FWHM) intensity of the bright peaks and the size of the crystalline regions was calculated as the distance between adjacent peaks at half their maximum intensity. The crystalline (dark) regions were 40 – 400 nm in length ($\bar{x}$: 190 nm, s.d.: 110 nm, Figure 3e), while the disordered (bright) regions were considerably shorter, measuring 20 – 120 nm in length ($\bar{x}$: 70 nm, s.d.: 30 nm, **Figure 3f**). The size of the crystalline regions is comparable to the reported length of CNCs produced through strong acid hydrolysis from bacterial and plant cellulose. Additionally, the "dark" fraction of the fibrils (73%) closely matches the reported yields of bacterial CNCs (78%) produced using similar hydrolysis conditions.[42] These observations suggest a correlation between the frequency and size of the dislocations and the final size of CNCs.

We next studied the effects of strong acid hydrolysis on the morphology and structure of CNCs to determine how the more accessible dislocations (bright regions) relate to the process of CNC isolation. To this end, sulfuric acid hydrolysis experiments were conducted on BC fibrils purified from *nata de coco*, where the acid concentration (64% w/w), temperature (70°C), and reaction time were tightly controlled. The dimensions and crystallinity of the resulting CNCs were characterized by TEM, AFM and XRD (**Figure 4**). After only 2 or 5 minutes of hydrolysis, BC cleaved to produce CNCs with lengths that spanned from 50 to 1000 nm (**Figure 4a**). Longer hydrolysis times resulted in a progressive shortening of the CNCs and a more homogenous distribution, which eventually levelled off at 70 – 500 nm ($\bar{x}$: 210 nm, s.d.:160 nm) after 60 minutes of hydrolysis (the typical time used for the production of CNCs).[43,44] Previous studies have observed longer particles ($\bar{x}$: 1000 nm) and higher dispersity (s.d.: 700 nm) in BC-derived CNCs,[45] which can be ascribed to the use of lower sulfuric acid concentrations[45–47] and temperatures[48], conditions that are known to significantly impact the rate of cellulose hydrolysis and the CNC yield.[49,50] We attribute the ability to control the length of CNCs and to observe the transition from a highly heterogeneous mixture of nanocrystal lengths to a more uniform population (similar to

those obtained through hydrolysis of cotton linters or filter paper) to the use of freeze-dried BC as a starting material, which allowed us to precisely control the sulfuric acid concentration and acid/cellulose ratio. The CNC cross-section, as measured by AFM height analysis (**Figure 4b** and **Figure S4**), decreased from 50 nm for untreated BC to 11 nm after only 2 minutes of hydrolysis, but did not change significantly with longer hydrolysis times. This is also in agreement with previous reports that show that CNCs produced from a variety of cellulose sources do not show changes in cross-section with increasing hydrolysis "harshness" (i.e., reaction time, temperature, acid/cellulose ratio, acid strength).[51,52] Furthermore, the crystallinity of cellulose did not change (within error) after acid hydrolysis and remained at > 90% even for longer hydrolysis times (**Figure 4b**). These results show that the cleavage of the BC fibrils into CNCs can be followed in detail by carefully controlling the hydrolysis time and reaction conditions.

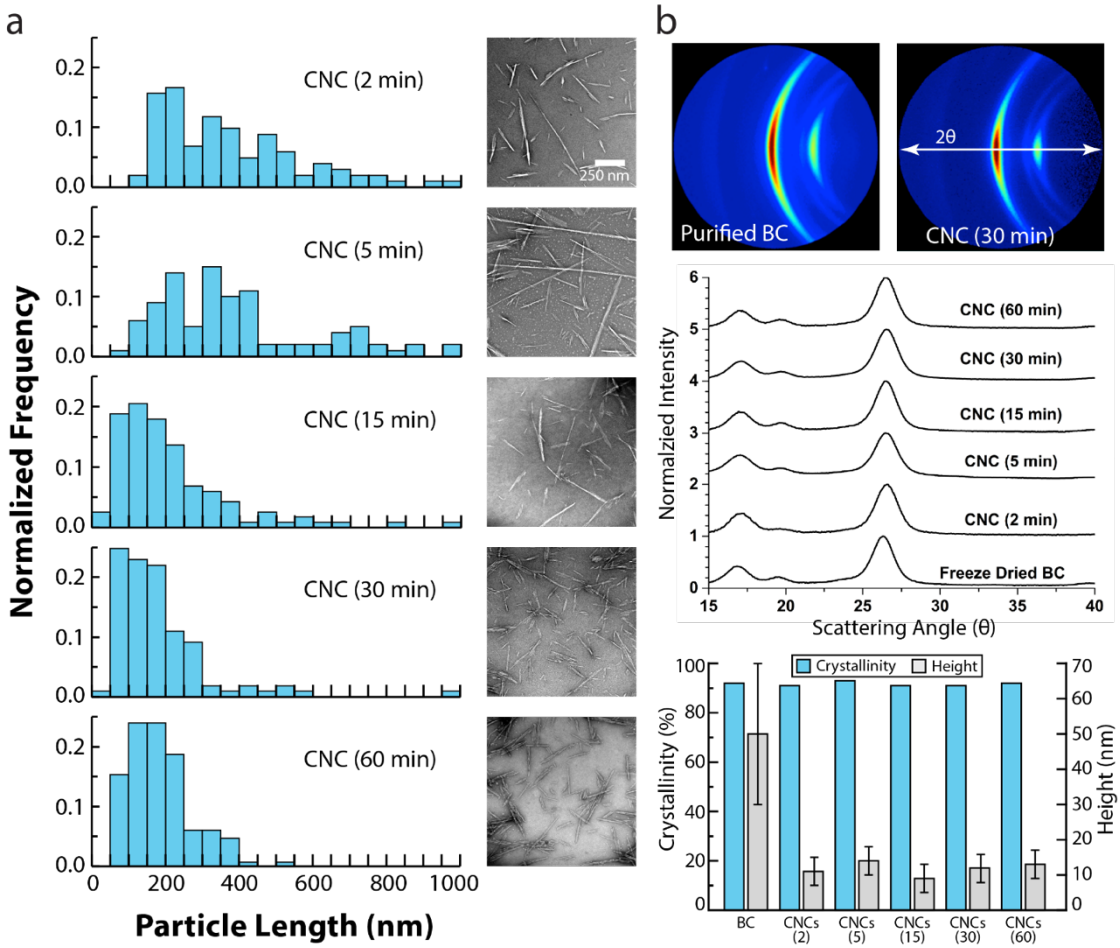

Figure 4. Length distribution, crystallinity, and height of CNCs produced from time-lapsed hydrolysis of bacterial cellulose. BC was hydrolysed with sulfuric acid (70°C, 64% (w/w) H_2SO_4, 4.0 g freeze-dried BC, 10:1 acid-to-cellulose ratio) for various durations until the reaction was quenched using a 10-fold dilution with water. **a)** The length of the CNCs was measured with TEM (N ≥ 100) and became shorter and more narrowly distributed with increasing hydrolysis times. **b)** Cellulose Iα percent crystallinity (%Cr) was calculated from one-dimensional X-ray diffraction plots using the peak deconvolution method. Triplicate %Cr measurements for CNC samples from 15- and 30-minute hydrolysis yielded a standard deviation of ± 2% and ± 1%. BC and CNC cross-sections were determined through AFM height measurements (N ≥ 100, error bars represent s.d.).

The distribution of the lengths of the sparsely labeled regions showed strong correlation and almost perfect overlap with the distribution of the length of CNCs produced from BC after 15 minutes of sulfuric acid hydrolysis (**Figure 3e** and **Figure S5**). This strongly suggests that the labeling pattern and the production of CNCs originate from the same process imposed by repeating regions of higher accessibility present along the length of the mostly crystalline BC fibrils. Similar to how these regions allow a high density of fluorophores to graft onto cellulose, they also act as vulnerable sites for acid hydrolysis and, in turn, fibril cleavage to produce CNCs. However, super-resolution microscopy results show that the dislocations can vary widely in accessibility, as evidenced by the two orders of magnitude spanned by the number of localizations identified within individual brightly labeled regions (**Figure 3c** and **Figure S5a**). Measuring the distance between the more accessible dislocations, by setting a higher peak-picking threshold (from 1× to 15× of fibril median intensity), resulted in dark regions that were longer and had a broader length distribution (**Figure S5b**), which matched the length distribution of CNCs produced by shorter acid hydrolysis times (**Figure S5c**).

When combining the CNC length measurements with the super-resolution microscopy results, we conclude that the strong acid treatment initially targets the larger, most accessible (more brightly labeled) disordered regions and quickly hydrolyzes these sites to create long CNCs with a large size dispersity (**Figure S6**). As the cellulose is further exposed to acid, the smaller dislocations are hydrolyzed. This results in additional cleaving of the cellulose particles, shortening their average length and decreasing their dispersity. Once all the intervening dislocations are cleaved, continued exposure to acid results in a progressive shortening of the CNCs as they are hydrolyzed from the ends. Through super-resolution imaging, it is possible to simultaneously visualize dislocations of varying size and degree of accessibility along the length of cellulose fibrils. Measuring the distance between all the dislocations, both large and small, provides a distribution that strongly correlates with that of the length of CNCs produced after prolonged hydrolysis times. These results shed light on the mechanism behind the extraction of CNCs and provide strong evidence of the persistent occurrence of dislocations or disordered regions along bacterial cellulose fibrils.

Overall, our results strongly support the fringed-micelle model of cellulose supramolecular structure, where fibrils are composed of highly crystalline portions – or micelles – interspersed with disordered domains – or fringes – that are more accessible and more susceptible to acid hydrolysis.[8,19] Originally, this model was proposed based on the observations of leveling-off in the degree of polymerization (LODP) of glucan chains following prolonged acidic hydrolysis.[17] The LODP of glucan chains from ramie fibers has further been correlated with SANS measurements that detected periodic cellulose disordered regions spaced every 150 nm along the fibril.[22] Our results show that in bacterial cellulose, the size of the crystalline regions exhibit non-uniform distribution and are larger than those reported in ramie fibers, with crystalline regions that can be as long as 500 nm. These observations are consistent with measurements that show that CNCs produced from bacterial cellulose are longer and have a broader distribution than those produced from plant material.[4,33,53] However, to our knowledge, there is no study that compares the length of CNCs produced from different sources of cellulose using the same hydrolysis conditions, something that we will aim to address in subsequent studies. The length of bacterial CNCs appears to be highly sensitive to acid hydrolysis conditions, with reported average length values between 200 and 1200 nm,[42,45] while plant-derived CNCs consistently yield 150 – 300 nm-long CNCs despite large variations in temperature and acid concentration.[45,50,52] These inconsistencies may be

attributed to differences in the supramolecular structures of bacterial and plant cellulose fibrils, where bacterial fibrils are organized into more complex hierarchical structures by a linear array of cellulose synthase terminal complexes that assemble cellulose into microfibrils, bundles and 50 nm wide ribbons.[32] Thus, the acidic hydrolysis of bacterial CNCs may also involve the defibrillation of ribbons into microfibril bundles, as seen by the width reduction of BC from 50 nm to 12 nm upon hydrolysis. In contrast, plant celluloses often undergo rigorous mechanical and chemical pre-treatment for defibrillation and lignin removal, which may increase their susceptibility to hydrolysis and in turn result in shorter CNCs.

An alternative, core-shell model has been proposed based on interpretations made from SANS, FT-IR, and solid-state NMR measurements, where the disordered fraction within cellulose fibrils resides mostly on the surface of the crystalline regions.[9,25] Additional support for this model has been derived from kink angle and persistence length measurements of TEMPO-oxidized wood cellulose nanofibrils,[26] where the non-normal distribution of kink angles was taken as evidence that the kinks could not represent intervening disordered regions within the fibril, but were instead a result of the high energy mechanical treatment that the materials were subjected to within a microfluidizer. Our data suggests that the disordered regions, which may be as subtle as the dislocation of a single glucan chain, create significant accessibility pockets. Thus, this is compatible with the observations made on TEMPO oxidized nanofibrils since such minor dislocations are not expected to have a significant impact on the flexibility (or modulus) of the fibrils or be the source of kinks. The remarkable contrast in intensity observed in the labeling pattern, the concomitant reduction in the length of CNCs due to acid hydrolysis and their constant cross-section strongly suggests that the intervening disordered regions reside along the fibrillar axis and have significantly higher accessibility than surface chains.

Compared to the crystalline regions, the size of the disordered regions has been more elusive as they are quickly hydrolyzed and are challenging to image by high-resolution microscopies like TEM and AFM. Through fluorescence labeling, super-resolution fluorescence microscopy allowed the visualization of the disordered regions and showed that they are almost three-fold smaller than the crystalline segments in the cellulose fibrils. However, the measured average length of 70 nm is significantly larger than what has been previously reported by SANS (2.5 nm)[22] and molecular dynamics simulations (~4 nm).[54] There are several reasons that account for this discrepancy; primarily, the length reported by Nishiyama was calculated from the initial mass loss and LODP of cellulose during hydrolysis, and assumed that the disordered regions span the entire cross-section of a fibril. Yet, this mass can be distributed over longer distances if it is limited to the chains closest to the surface of the fibril, which would be consistent with the predictions of the core-shell model and result in longer measured lengths of the disordered regions. At the same time, the bright regions observed along the fibrils could represent multiple dislocations within individual bundles or microfibrils that are slightly offset and give rise to a longer perceived length of the disordered regions. Since the resolution of STORM is limited to ~30 nm, visualizing the ultrastructure of the disordered regions beyond the cross-section of the thin fibrils (also ~30 nm) is challenging. This limitation is further compounded by the high labeling density of the disordered regions, which can result in overcrowded emissions during the STORM acquisition and could lead to imaging artifacts that overestimate the true size of the disordered regions. However, the length of the disordered regions within bacterial cellulose is still unlikely to be as small as 2 – 4 nm given the strong correlation observed between the measured lengths of the dark regions and CNCs. While the disordered regions of plant cellulose fibrils may be smaller than those of bacterial cellulose, a

recent study that visualized the hydrolysis of plant cellulose suggested that the disordered regions can be as large as 20 nm, in good agreement with the length scales we observed.[55]

The presence of non-crystalline components within cellulose has been assessed from XRD diffractograms, frequently through a deconvolution method that includes a broad baseline peak.[56] Using this approach, we measured the crystallinity of BC to be ~90%, and found that this number did not increase significantly following the cleavage of the fibrils into CNCs or after extended hydrolysis times.[27] This suggests that the disordered regions, despite being on average 70 nm long and being present on 27% of the fibril length, do not consist of fully amorphous cellulose. Instead, disordered regions are most likely in the form of misaligned (i.e., dislocated) glucan chains or nanostructural defects in the crystalline network at the sub-fibril level, rather than highly disordered or fully amorphous cellulose. This assessment is further supported by our observation that cellulases, with 5-10 nm hydrodynamic radii, do not show preferential binding or localization on the dislocations, which would be expected for amorphous cellulose as discussed further below (**Figure 5**).[57]

Although the results presented here are derived from experiments with bacterial cellulose as a model substrate, we propose that super-resolution microscopy could be similarly applied to study celluloses derived from other sources. This method has the advantage of being able to directly visualize and quantify regions with different degrees of order in a hydrated state. Thus, subsequent studies could focus on a detailed assessment of cellulose fibrils from other sources, such as plant, tunicates and algae, or on the impact of chemical and biological treatments on the nanostructure of cellulose fibrils. The direct visualization of the fringed-micellar structure on a fibril-by-fibril basis could reveal similar heterogeneities in the spacings and accessibility of the disordered regions within plant cellulose. However, the resolution of SRFM is still limited to tens of nanometers, preventing a more in depth understanding of the structure of the disordered regions and their relationship to the hierarchical organization of cellulose, particularly within the individual bundles and microfibrils. This limitation, combined with the stochastic nature of SRFM, could overestimate the true heterogeneity of cellulose dislocations, particularly if the dislocations exist at the bundle or microfibril level. This technique could thus be complemented with higher resolution microscopies such as TEM and AFM in a correlative imaging workflow to gain ultrastructural context.

The non-normal distribution of the spacings and intensities from the pattern seen on labelled BC fibrils indicate that the dislocations are heterogenous and their presence may not be the product of a controlled, canonical biological process. It is possible that they arise from built up tension or "seizing" of the molecular machinery at work in the biosynthesis of cellulose fibrils. In *K. xylinum*, the bacterial cellulose is synthesized by a cellulose synthase complex – or terminal complexes (TC) – that span across the inner and outer membranes while in a linear arrangement along the surface of the bacterium.[58] Downstream of the *acsAB* glucose transferase enzyme, which appends anhydroglucose units to the nascent glucan chain, *acsD* and *acsC* are presumed to be responsible for exporting the glucan chains and crystallizing them into elementary fibrils, respectively.[59] Errors during this final step of the process could introduce misalignment between the glucan chains and thus be responsible for the prevalence of dislocations. The crystal structure of *acsC* has shown that this protein can simultaneously bind four cellopentose chains with a weak affinity through four helical passageways.[60] TCs missing this enzyme, or where the enzyme is transiently inactive, may generate interspersed dislocations. Moreover, previous molecular dynamics have shown that the intrinsic chiral twist in a cellulose fibril, arising from the crystalline packing, introduces tension

on the outer chains of a cellulose fibril.[61] This strain could be relaxed by introducing misalignments and dislocations that could cause small breaks in the crystalline structure. [61]

There has been much speculation on the biological relevance of dislocations within crystalline cellulose fibrils. In bacteria, the dislocations are suspected to create water-accessible pockets that can partially swell the fibrils and enhance the flotation of the cellulose mats, which bacteria exploit to gain increased exposure to oxygen.[22,62] In plants, the dislocations could provide active sites for hydrogen-bond disrupting proteins like expansins and swollenins, which have been shown to weaken cellulose fibers and increase their hydrolysis by cellulases.[63] It has also been speculated that disordered regions could be created by the integration of hemicellulose within the fibril during its assembly, creating defects in the crystalline structure at that region.[64,65] Membrane-bound endoglucanses, which can break glycosidic linkages within a cellulose chain could act on these sites to release the fibril from its association with hemicellulose and weaken its interaction to its surrounding matrix.[66,67] These processes have been shown to play a significant role in the relaxation and the remodelling of plant cell walls as they expand and change shape, highlighting the biological importance of nanoscale dislocations within cellulose fibrils.[66] An additional implication of these nanostructural features is that they could create hotspots for cellulase binding, enhancing the ability of these enzymes to depolymerize the glucan chains into soluble sugars. To investigate this possibility, we incubated AF647-labeled *Trichoderma reseii* Cel7A – which retains enzymatic activity similar to that of its unlabelled counterpart[68] – with DTAF-labeled BC and acquired two-color super-resolution images. Analysis of the intensity profiles from the two channels revealed that the enzymes did not exhibit enhanced binding at the dislocations in the fibrils (**Figure 5**). Enhanced binding is expected in amorphous cellulose given that the enzyme's carbohydrate binding module tethers it randomly to the hydrophobic facet of cellulose chains.[70] This observation implies that the disorder introduced by the dislocations does not create pockets of amorphous cellulose large enough for enzymes 5-15 nm in size to experience enhanced binding. These results open the door for the deployment of multicolour super-resolution microscopy for the exploration of the impact of nanoscale structure and pre-treatment strategies on cellulase-cellulose interactions.

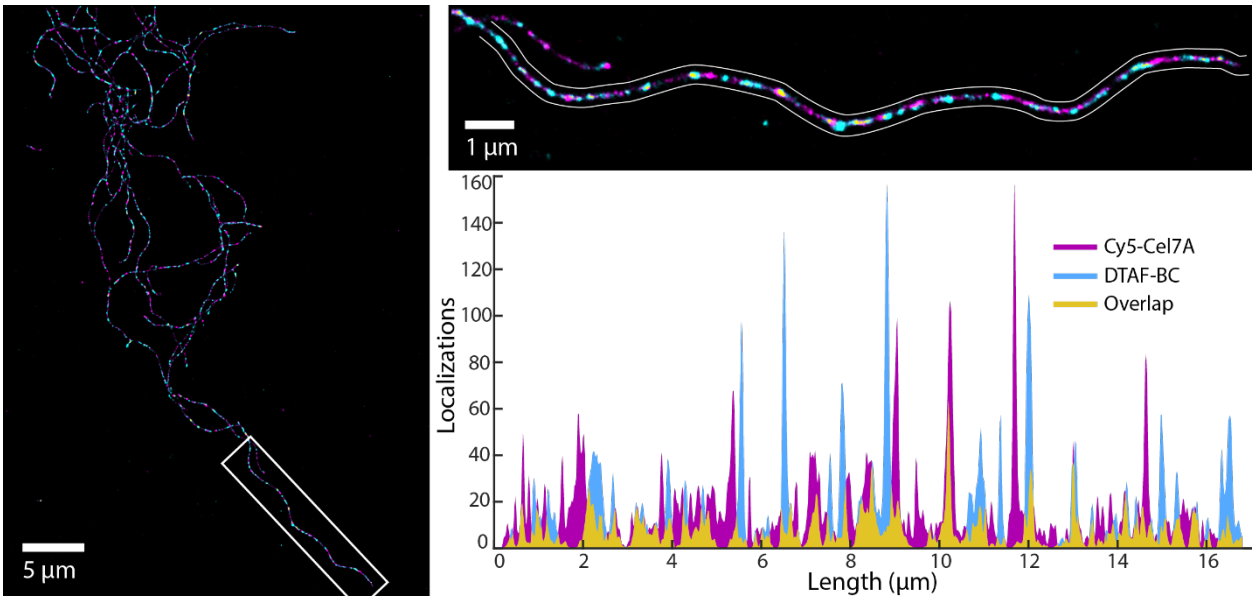

Figure 5. Two-colour super-resolution images of DTAF-labeled BC (blue) and bound AF647-Cel7A (magenta). AF647-Cel7A was incubated on DTAF-labeled BC at concentrations of 5 nM and super-resolution images were acquired at room temperature. Qualitative analysis of the colocalization of the dislocations and binding sites of Cel7A was done by highlighting overlapping regions of the intensity profiles of the fibril in the two-colour channels (shown in yellow). Super-resolution imaging showed that the cellulases did not exhibit preferential binding to either the disordered or crystalline regions, suggesting that the size of the disordered regions is not large enough (>10 nm) to enhance enzyme binding.

CONCLUSION

The presence of an alternating crystalline and disordered structure along cellulose fibrils has been a topic of much debate within the field of cellulose research, as this structure cannot be directly visualized by techniques conventionally used to study the supramolecular organization of cellulose. By leveraging the process of fluorescence labeling to probe variations in accessibility of glucan chain hydroxyl groups, we used super-resolution fluorescence microscopy to visualize a repeating pattern of nanoscale dislocations along bacterial cellulose fibrils. The microscopy data shows that these dislocations are heterogenous in size, separation distance, and accessibility. Through crystallinity and length measurements of CNCs produced from the controlled acid hydrolysis of cellulose fibrils, we show how these dislocations govern the production and final size distribution of CNCs. The unchanged crystallinity of cellulose following acid hydrolysis and the non-preferential binding of cellulase Cel7A to the dislocations also implies that while these dislocations create ~70 nm pockets of accessibility for small molecules, they do not constitute fully amorphous regions that would allow macromolecules, like cellulases with sizes > 5 nm, to exhibit enhanced binding to dislocations. The ability to visualize dislocations on cellulose fibrils can act as a platform to detect amorphogenesis at the nanoscale, opening the door for future work on understanding how various proteins, enzymes and chemical agents can alter the structure of cellulose at the fibril level. Understanding the nanostructure of cellulose and how it is altered through different treatments is critical for understanding its biological role and for the development of new sustainable nanomaterials, biofuels, and bioplastics.

MATERIALS & METHODS

Nata de coco (230 g drained weight, New Lamthong Food Industries, Bangkok, Thailand) was purchased from a local Asian foods store. Rhodamine 6G (95%), 6-aminofluorescein (95%), cyanuric chloride (99 %), phosphorus oxychloride ($POCl_3$, 99%), piperazine (99 %), glucose oxidase (from *Aspergillus niger*, type X−S, 100−250 units/mg, 65−85% protein content), catalase (from bovine liver, ≥10 000 units/mg, ≥70% protein content), and cysteamine hydrochloride (≥98%) were purchased from MilliporeSigma (Oakville, ON, Canada) and used as is. Avicel 101 was purchased from MilliporeSigma (St. Louis, MO). FAM and sulfo-Cy5 azide (Cy5) were purchased from Lumiprobe (Hunt Valley, MD, USA). Poly(allylamine hydrochloride) was purchased from Polysciences Inc. (Warrington, PA, USA) and had a nominal molecular weight of 120-200 kDa. Glass-bottom petri dishes were purchased from MatTek (Ashland, MA). *Thermofibda fusca* Cel7A was expressed, purified, and labelled with Alexa-Fluor 647 to a degree of labeling of 2.95, as described previously.[68] DTAF, DTPR and DTAP were synthesized in-house as previously reported.[69] All mentions of water refer to deionized 18.2 MΩ water generated from a Milli-Q purification system (Millipore Sigma).

Nata de coco purification

Bacterial cellulose was purified from *nata de coco* foodstuff through a mild alkaline treatment, as previously reported.[69,70] Briefly, the dessert was drained and thoroughly rinsed with water before being blended in a Magic Bullet blender (Nutribullet, Los Angeles, CA, USA). The slurry was treated with 0.1 M NaOH for 20 min at 80 °C, then quenched with chilled water and rinsed with 7 cycles of centrifugation (1800*g*, 10 mins), decanting and resuspension in water until the pellet became white. The pellet was resuspended in water to a final concentration of 2 mg/mL for fluorescence labeling and characterization by super-resolution imaging, or freeze-dried and blended for 2 mins for the subsequent production of CNCs through controlled acid hydrolysis

Fluorescence labeling of BC

DTAF and DTPR triazine dyes are based on fluorescein and rhodamine 6G, respectively, and were used to label BC directly in one step by stirring a 5 mL solution of 0.1 M NaOH, 1 mg/mL BC and 1 mM of dye for 24 hrs. The samples were washed with 15 cycles of centrifugation (21,100×g, 30 s, Sorvall Legend Micro 21R Centrifuge, Thermo Scientific), decanting and resuspension in 1X PBS by vortexing. Samples were sonicated every third spindown using a ¼ inch point-probe (Branson SLPt, 40% amplitude, or 90 W, for 10 s) to disperse any cellulose that remained lumped even after vortexing. The sample was washed with water for 5 cycles to ensure all the buffer was removed and the volume was adjusted to reach a final cellulose concentration of 1 mg/mL.

To achieve higher degrees of labeling, BC was also labeled with FAM azide or Cy5 azide dyes using a previously developed two-step labeling scheme that relies on a DTAP triazine linker possessing an alkyne group.[37,69] Briefly, a 5 mL solution of 3:1 water:acetone containing 0.05 M NaOH, 1 mg/mL BC and 10 mM DTAP was mixed using a rotating mixer for 24 hrs. Similarly to the previous cleaning procedure, the suspension was cleaned by centrifugation cycles 3 times with water, 3 times with acetone, 3 times with 1X PBS then 3 times with water and diluted to a final cellulose concentration of 1 mg/mL. The DTAP-functionalized BC was then labeled through a copper-catalyzed azide-alkyne cycloaddition click-reaction with either Cy5 or FAM by mixing a 1X PBS (for Cy5) or 1:1 water:methanol (for FAM) solution of 1 mg/mL of DTAP-BC containing

1 mM of FAM or 5 µM of Cy5 or 10 µM of Cy5, 0.3 mM $CuSO_4 \cdot 5H_2O$ and 5 mM ascorbic acid for 24 hours. The Cy5-BC sample was cleaned with a minimum of 10 cycles of water washing, centrifugation, decanting and resuspension, while FAM-BC was cleaned with 5 washing cycles of 50% methanol, 3 cycles of PBS and 3 cycles of water washing and diluted to a final cellulose concentration of 1 mg/mL.

Super-resolution microscopy of cellulose fibrils

All cellulose samples were prepared on MatTek glass-bottom petri dishes by drop casting 100 µL of a ~0.1 mg/mL solution of labelled BC and drying at 70 ºC. Prior to imaging, all samples were washed three times with water and STORM switching buffer was added (50 mM Tris, pH 8.0, 10 mM NaCl, 10% glucose w/w, cysteamine, 0.56 mg/mL (56 u/mL) glucose oxidase and 40 µg/mL (381 u/mL) catalase). The concentration of cysteamine used for imaging DTAF-BC, $Cy5_{10\ \mu M}$-BC and $Cy5_{10\ \mu M}$-BC were 100 mM, 100 mM and 50 mM, respectively.

Super-resolution fluorescence microscopy was carried out as previously described.[69] Briefly, images were acquired on a Leica DMI6000 B inverted fluorescence microscope equipped with a 100x/1.47NA oil-immersion objective. Widefield illumination was achieved using a Borealis illumination module (Spectral Applied Research, Richmond Hill, ON, Canada) that is coupled to four solid-state laser lines (405, 488, 561 and 647 nm). Emission and illumination light were separated by multiline dichroic mirror and different colour channels were split by a 640 nm dichroic mirror into two light paths. Fluorescence light was further filtered through the appropriate color filter (460/50, 525/50, 593/40 or 700/75 nm) before being captured by one of two iXon Ultra DU-897U EMCCD cameras (10 MHz readout mode, frame transfer ON, 3.30 µs vertical clock speed, electron-multiplying mode) with a 96.1 nm projected pixel size

Diffraction-limited, well-dispersed and dim fibrils, as such to avoid wide ribbons, were selectively imaged using STORM by illuminating the sample with 0.72 kW/cm^2 of 488 nm light for DTAF-BC, 0.41 kW/cm^2 of 640 nm light for $Cy5_{5\ \mu M}$-BC and 0.48 kW/cm^2 of 640 nm light for $Cy5_{10\ \mu M}$-BC. An image sequence of 6000 frames for DTAF-BC or 24,000 frames for Cy5-BC was acquired with an exposure time of 30 ms (30 Hz actual frame rate). For samples labelled with Cy5, fluorophores were occasionally reactivated with a fixed, pre-recorded pulse sequence of 405 nm laser at 0.38 – 4.10 mW/cm^2 illumination power to optimize the emission density within the dimmest cellulose fibrils. Average localization uncertainties were approximately 14 nm for Cy5-BC and 18 nm for DTAF-BC, respectively.

Image and data analysis

Image stacks were cropped to a time point where individual, discernable single molecule emission can be seen on the fibrils, which was at 3,000 for DTAF-BC and $Cy5_{5\ \mu M}$-BC or 4,000 for $Cy5_{10\ \mu M}$-BC. STORM single-molecule analysis and image reconstruction were performed using the ThunderSTORM ImageJ plugin. Here, a B-spline wavelet filter was used to enhance the contrast of single-molecules to approximate their position through the local maximum method. Sub-pixel localization was performed by fitting a 2-dimesional integrated Gaussian function using the weighted least squares method.[71] Single emitter molecule localizations were further filtered using the following parameters: sigma<(mean(sigma)+std(sigma)) & sigma>(mean(sigma)-std(sigma*1.3)) & uncertainty<40 nm & uncertainty >5 nm & intensity<2500 photons. Consecutive emissions (with an OFF tolerance of 1 frame) within a 20 nm radius were merged. Sample drift was corrected using the cross-correlation method and the super-resolution image was

rendered with a magnification factor of 5 (19.2 nm pixel size) or 10 (9.6 nm pixel size) for DTAF-BC and Cy5-BC samples, respectively. Two-colour images of enzyme-bound BC were aligned and corrected for chromatic aberration using a displacement correction map generated by the Detection of Molecules (DoM v.1.2.0, Cell Biology group at Utrecht University) ImageJ plugin following the analysis of a Tetraspeck bead standard sample.

Using the ImageJ segmented line tool, isolated and dim fibrils from at least twenty acquisitions of each sample were traced using a spline-fitted line with a width value of 18 pixels for DTAF-BC or 40 pixels for Cy5-BC. An intensity profile was acquired and imported into MATLAB (MathWorks, Massachusetts) for further analysis using a custom-written script. Here, the 'findpeaks' function was used to identify the location and width of bright emission peaks, using threshold values of 40 nm inter-peak distance and 20 nm peak width. The peak prominence threshold was determined using one of two methods. The global thresholding method relied on the background population seen in the cumulated intensity distribution of all fibril profiles (Figure S3). In DTAF-BC fibrils, the image background was representative of the dark regions and three standard deviations above this population, which was determined through a bimodal fitting of the distribution, of 1.2 localizations was used. The second method was a local thresholding method based on the median peak prominence of all local maxima present in a profile. Without any thresholds, the "findpeaks" function was used to identify all local maxima and the median prominence of the identified peaks was used as the prominence threshold, in conjunction with 40 nm inter-peak distance and 20 nm peak width thresholds, to identify peaks that were representative of the bright regions (Figure S2). Peaks with a signal-to-background ratio below 2 were discarded. Using the peak position and widths that were determined through either of these thresholding methods, the length of the dark regions was calculated using the following equation, where x_i is the position of the ith peak:

$$Spacing\ length = x_{i+1} + \frac{FWHM_{i+1}}{2} - \left(x_i + \frac{FWHM_i}{2}\right) \qquad \textbf{(Equation 3)}$$

Spacing values lower than 20 nm were discarded, as this was the lower bound resolution of our super-resolution images.

Sulfuric acid hydrolysis of bacterial cellulose

In a water bath, 65% H_2SO_4 (w/w) was heated to 70°C and then 4.0 g of freeze-dried BC was added with continuous mechanical stirring (final acid to cellulose ratio = 10 mL/g). Hydrolysis reaction times were varied from 2–60 minutes (as listed in Table 1) and all other conditions were kept constant. The hydrolyzed slurries were quenched in 10x volume of chilled water and allowed to equilibrate to RT. Cycles of centrifugation (1800*g*, 10-15 minute), decanting, and resuspension in water were used to remove the acid from the reaction mixture until the cellulose pellet was no longer stable (~4 rinses). The suspensions were extensively dialyzed (using Spectra Por dialysis tubing with 14 kDa MWCO from Sigma-Aldrich) against water for 2-3 weeks, with daily water changes, until constant pH. The suspensions were then sonicated for 2-3 minutes at 60% amplitude (equivalent to 90W, Sonifier 450; Branson Ultrasonics, Danbury, CT), and concentrated to ~1 wt% using an ultrafiltration stirred cell operating at ~140 kPa N_2 pressure (solvent-resistant stirred cell fitted with 76 mm ultrafiltration discs; Millipore). The resulting suspensions were stored in acid-form at 4 ºC.

Conductometric titrations

Sulfuric acid hydrolysis of cellulose results in the formation of sulfate half-ester groups on the surface of CNCs that deprotonate under all working conditions to impart a negative charge. To determine the CNC sulfur content, 0.1 g of CNCs were added to 75 mL of 1 mM NaCl solution (used to increase the baseline conductivity of the suspension) and titrated with 2 mM NaOH. Injections of 0.2 mL of titrant were added every 30 seconds and the conductivity was measured upon each addition. An auto-titrator (Mandel, Man-Tech PLM-100214) was used with a Man-Tech 991 electrode, and titrations were done in triplicate for each suspension. The sulfur content (R-OSO_3H, mmol/kg CNC) was calculated from the equivalence point of the titration through the following equation[72]:

$$\text{R-OSO}_3\text{H} = \frac{(V_{NaOH}C_{NaOH})}{V_{susp}C_{susp}} \times \frac{1000\ g}{1\ kg} \qquad \textbf{(Equation 4)}$$

Where V_{NaOH} is the volume of base used to reach the equivalence point, C_{NaOH} is the millimolar concentration of base, V_{susp} is the volume of the CNC suspension in L, and C_{susp} is the CNC concentration in g/L. The CNC sulfur content is summarized in **Table S1**.

Transmission electron microscopy (TEM)

Images of CNC samples were obtained using a JEOL JEM 1200 EX TEMSCAN Transmission Electron Microscope operating at 56 kV. CNC suspensions (3.5 µL, 0.001% w/w) were dried onto freshly prepared 200-mesh carbon coated Cu grids. Grids were glow discharged prior to use in order to improve material dispersion. The grids were then stained with a 1% (w/v) solution of uranyl acetate for 2 minutes.

Atomic force microscopy (AFM)

Square silicon wafer pieces (~1 cm^2) were cleaned using Piranha (3:1 H_2SO_4 (12M):H_2O_2 (30%)) and then thoroughly rinsed with water prior to use. Using a spin coater, 0.1 wt% polyallylamine hydrochloride was deposited onto each square followed by a rinse with water. Then, a drop of 0.01 wt% CNC suspension was spin-coated at 3000 rpm for 30 seconds in a G3P-12 Spin Coater (Specialty Coating Services, Indianapolis, IN), and a final rinse with water was performed. Images were acquired in tapping mode using a Nanoscope IIIa Multimode Scanning probe Microscope with cantilevers from Asylum Research (AC160TS type, 42 N/m spring constant, and 300 kHz nominal resonance frequency).

X-Ray diffraction

Two-dimensional diffraction patterns were collected using a D8 Davinci diffractometer (Bruker, Billerica, MA) equipped with a sealed tube cobalt source (note: cobalt source, not the more conventional copper). All analysis of the resulting patterns was conducted using the Bruker TOPAS software. The beam was collimated to a diameter of 0.5 mm (35mA, 45kV). Cellulose samples were drop-cast and oven dried onto clean Si wafer pieces for the analysis. A still frame of a blank piece of Si was initially examined to correct for background. The background intensity was subtracted from each sample frame prior to integration of the data. A 2θ range of 13–42° was used for the percent crystallinity (%Cr) analysis. Integration along relative angle χ for every 2θ value was performed to obtain one-dimensional diffraction plots of intensity versus 2θ (cf. wireframe in Figure 4b). The background corrected intensity vs. 2θ plots were fitted to five

symmetric Lorentzian peaks, four peaks corresponding to the (100), (010), (002), and (040) crystalline planes[73], and one broad amorphous peak fixed at 24.1°. The %Cr was calculated by the peak deconvolution method as the ratio of the area for the crystalline peaks over the total area for the diffraction plots. The deconvolution method was validated by analysing the %Cr of an Avicel 101 reference sample, which yielded a %Cr value of 75%.

Enzyme binding assays

For enzyme binding experiments, dried DTAF-BC samples were blocked with 3 mL of 10 mg/mL BSA (purified using a 0.045 µm syringe filter) in sodium acetate buffer (50 mM, pH 5.0) and incubated overnight. The sample was then washed three times with buffer and incubated with 2 mL of 5 nM AF647-Cel7A for 2 hours at 4 ºC in sodium acetate buffer. Prior to SRFM imaging, the sample was washed three times with water and STORM switching buffer was added (50 mM Tris 50, pH 8.0, 10 mM NaCl, 10% glucose w/w, 100 mM cysteamine, 0.56 mg/mL (56 u/mL) glucose oxidase and 40 µg/mL (381 u/mL) catalase).

REFERENCES

1. Klemm, D., Heublein, B., Fink, H. P. & Bohn, A. Cellulose: Fascinating biopolymer and sustainable raw material. *Angewandte Chemie - International Edition* **44**, 3358–3393 (2005).

2. Bar-On, Y. M., Phillips, R. & Milo, R. The biomass distribution on Earth. *Proceedings of the National Academy of Sciences* **115**, 6506–6511 (2018).

3. Paajanen, A., Ceccherini, S., Maloney, T. & Ketoja, J. A. Chirality and bound water in the hierarchical cellulose structure. *Cellulose* **26**, 5877–5892 (2019).

4. Habibi, Y., Lucia, L. A. & Rojas, O. J. Cellulose nanocrystals: Chemistry, self-assembly, and applications. *Chemical Reviews* **110**, 3479–3500 (2010).

5. Habibi, Y. Key advances in the chemical modification of nanocelluloses. *Chem Soc Rev* **43**, 1519–42 (2014).

6. Himmel, M. E. *et al.* Biomass recalcitrance: Engineering plants and enzymes for biofuels production. *Science* **315**, 804–807 (2007).

7. Moran-Mirabal, J. M. The study of cell wall structure and cellulose-cellulase interactions through fluorescence microscopy. *Cellulose* **20**, 2291–2309 (2013).

8. Hon, D. N. S. Cellulose: a random walk along its historical path. *Cellulose* **1**, 1–25 (1994).

9. Fernandes, A. N. *et al.* Nanostructure of cellulose microfibrils in spruce wood. *Proc Natl Acad Sci U S A* **108**, 1195–1203 (2011).

10. Nishiyama, Y. Structure and properties of the cellulose microfibril. *Journal of Wood Science* **55**, 241–249 (2009).

11. Song, B., Zhao, S., Shen, W., Collings, C. & Ding, S.-Y. Direct measurement of plant cellulose microfibril and bundles in native cell walls. *Frontiers in Plant Science* **11**, 479 (2020).

12. Rose, M., Babi, M. & Moran-Mirabal, J. The study of cellulose structure and depolymerization through single-molecule Methods. *Industrial Biotechnology* **11**, 16–23 (2015).

13. Ding, S. Y., Zhao, S. & Zeng, Y. Size, shape, and arrangement of native cellulose fibrils in maize cell walls. *Cellulose* **21**, 863–871 (2014).

14. Gill, U. *et al.* Beyond buckling: Humidity-independent measurement of the mechanical properties of green nanobiocomposite films. *Nanoscale* **9**, 7781–7790 (2017).

15. Altaner, C. M., Thomas, L. H., Fernandes, A. N. & Jarvis, M. C. How cellulose stretches: Synergism between covalent and hydrogen bonding. *Biomacromolecules* **15**, 791–798 (2014).

16. Nickerson, R. F. & Habrle, J. A. Cellulose intercrystalline structure. *Industrial & Engineering Chemistry* **39**, 1507–1512 (1947).

17. Battista, O. A. Hydrolysis and crystallization of cellulose. *Industrial & Engineering Chemistry* **42**, 502–507 (1950).

18. Battista, A., Coppicic, S., Howsmon, J. A., Morehead, F. F. & Sisson, W. A. Level-off degree of polymerization: relation to polyphase structure of cellulose fibrils. *Industrial & Engineering Chemistry* **48**, 333–335 (1956).

19. Scallan, A. M. A quantitative picture of the fringed micellar model of cellulose. *Textile Research Journal* **41**, 647–653 (1971).

20. Mariano, M., el Kissi, N. & Dufresne, A. Cellulose nanocrystals and related nanocomposites: Review of some properties and challenges. *Journal of Polymer Science Part B: Polymer Physics* **52**, 791–806 (2014).

21. Salas, C., Nypelö, T., Rodriguez-Abreu, C., Carrillo, C. & Rojas, O. J. Nanocellulose properties and applications in colloids and interfaces. *Current Opinion in Colloid & Interface Science* **19**, 383–396 (2014).

22. Nishiyama, Y. *et al.* Periodic disorder along ramie cellulose microfibrils. *Biomacromolecules* **4**, 1013–1017 (2003).

23. Ciesielski, P. N. *et al.* Nanomechanics of cellulose deformation reveal molecular defects that facilitate natural deconstruction. *Proc Natl Acad Sci U S A* **116**, 9825–9830 (2019).

24. Rowland, S. P. & Roberts, E. J. The nature of accessible surfaces in the microstructure of cotton cellulose. *Journal of Polymer Science Part A-1: Polymer Chemistry* **10**, 2447–2461 (1972).

25. Martinez-Sanz, M., Gidley, M. J. & Gilbert, E. P. Hierarchical architecture of bacterial cellulose and composite plant cell wall polysaccharide hydrogels using small angle neutron scattering. *Soft Matter* **12**, 1534–1549 (2016).

26. Usov, I. *et al.* Understanding nanocellulose chirality and structure–properties relationship at the single fibril level. *Nature Communications* **6**, 7564 (2015).

27. Park, S., Baker, J. O., Himmel, M. E., Parilla, P. A. & Johnson, D. K. Cellulose crystallinity index: Measurement techniques and their impact on interpreting cellulase performance. *Biotechnology for Biofuels* **3**, 1–10 (2010).

28. van de Linde, S. *et al.* Direct stochastic optical reconstruction microscopy with standard fluorescent probes. *Nature Protocols* **6**, 991–1009 (2011).

29. Rust, M. J., Bates, M. & Zhuang, X. Sub-diffraction-limit imaging by stochastic optical reconstruction microscopy (STORM). *Nature Methods* **3**, 793–795 (2006).

30. Thevathasan, J. V. *et al.* Nuclear pores as versatile reference standards for quantitative superresolution microscopy. *Nature Methods* **16**, 1045–1053 (2019).

31. Singhsa, P., Narain, R. & Manuspiya, H. Physical structure variations of bacterial cellulose produced by different Komagataeibacter xylinus strains and carbon sources in static and agitated conditions. *Cellulose* **25**, 1571–1581 (2018).

32. Tokoh, C., Takabe, K., Fujita, M. & Saiki, H. Cellulose synthesized by Acetobacter xylinum in the presence of acetyl glucomannan. *Cellulose* **5**, 249–261 (1998).

33. Araki, J. & Kuga, S. Effect of trace electrolyte on liquid crystal type of cellulose microcrystals. *Langmuir* **17**, 4493–4496 (2001).

34. Mehta, K., Pfeffer, S. & Brown, R. M. Characterization of an acsD disruption mutant provides additional evidence for the hierarchical cell-directed self-assembly of cellulose in Gluconacetobacter xylinus. *Cellulose* **22**, 119–137 (2014).

35. Reid, M. S., Karlsson, M. & Abitbol, T. Fluorescently labeled cellulose nanofibrils for detection and loss analysis. *Carbohydrate Polymers* **250**, 116943 (2020).

36. Helbert, W., Chanzy, H., Husum, T. L., Schülein, M. & Ernst, S. Fluorescent cellulose microfibrils as substrate for the detection of cellulase activity. *Biomacromolecules* **4**, 481–487 (2003).

37. Fatona, A., Berry, R. M., Brook, M. A. & Moran-Mirabal, J. M. Versatile surface modification of cellulose fibers and cellulose nanocrystals through modular triazinyl chemistry. *Chemistry of Materials* **30**, 2424–2435 (2018).

38. Moran-Mirabal, J. M., Santhanam, N., Corgie, S. C., Craighead, H. G. & Walker, L. P. Immobilization of cellulose fibrils on solid substrates for cellulase-binding studies through quantitative fluorescence microscopy. *Biotechnology and Bioengineering* **101**, 1129–1141 (2008).

39. Luterbacher, J. S., Walker, L. P. & Moran-Mirabal, J. M. Observing and modeling BMCC degradation by commercial cellulase cocktails with fluorescently labeled Trichoderma reseii Cel7A through confocal microscopy. *Biotechnology and Bioengineering* **110**, 108–117 (2013).

40. Chen, P., Ogawa, Y., Nishiyama, Y., Ismail, A. E. & Mazeau, K. Linear, non-linear and plastic bending deformation of cellulose nanocrystals. *Physical Chemistry Chemical Physics* **18**, 19880–19887 (2016).

41. Dempsey, G. T., Vaughan, J. C., Chen, K. H., Bates, M. & Zhuang, X. Evaluation of fluorophores for optimal performance in localization- based super-resolution imaging. *Nature Methods* **8**, 1–44 (2011).

42. Singhsa, P., Narain, R. & Manuspiya, H. Bacterial cellulose nanocrystals (BCNC) preparation and characterization from three bacterial cellulose sources and development of functionalized BCNCs as nucleic acid delivery systems. *ACS Applied Nano Materials* **1**, 209–221 (2017).

43. Kargarzadeh, H. *et al.* Effects of hydrolysis conditions on the morphology, crystallinity, and thermal stability of cellulose nanocrystals extracted from kenaf bast fibers. *Cellulose* **19**, 855–866 (2012).

44. Reiniati, I., Hrymak, A. N. & Margaritis, A. Recent developments in the production and applications of bacterial cellulose fibers and nanocrystals. *Critical Reviews in Biotechnology* **37**, 510–524 (2017).

45. Sacui, I. A. *et al.* Comparison of the properties of cellulose nanocrystals and cellulose nanofibrils isolated from bacteria, tunicate, and wood processed using acid, enzymatic, mechanical, and oxidative methods. *ACS Applied Materials and Interfaces* **6**, 6127–6138 (2014).

46. Roman, M. & Winter, W. T. Effect of sulfate groups from sulfuric acid hydrolysis on the thermal degradation behavior of bacterial cellulose. *Biomacromolecules* **5**, 1671–1677 (2004).

47. Kalashnikova, I., Bizot, H., Bertoncini, P., Cathala, B. & Capron, I. Cellulosic nanorods of various aspect ratios for oil in water Pickering emulsions. *Soft Matter* **9**, 952–959 (2012).

48. Martínez-Sanz, M., Lopez-Rubio, A. & Lagaron, J. M. Optimization of the nanofabrication by acid hydrolysis of bacterial cellulose nanowhiskers. *Carbohydrate Polymers* **85**, 228–236 (2011).

49. Wang, Q., Zhao, X. & Zhu, J. Y. Kinetics of strong acid hydrolysis of a bleached kraft pulp for producing cellulose nanocrystals (CNCs). *Industrial and Engineering Chemistry Research* **53**, 11007–11014 (2014).

50. Chen, L. *et al.* Tailoring the yield and characteristics of wood cellulose nanocrystals (CNC) using concentrated acid hydrolysis. *Cellulose* **22**, 1753–1762 (2015).

51. Beck-Candanedo, S., Roman, M. & Gray, D. G. Effect of reaction conditions on the properties and behavior of wood cellulose nanocrystal suspensions. *Biomacromolecules* **6**, 1048–1054 (2005).

52. Vanderfleet, O. M., Osorio, D. A. & Cranston, E. D. Optimization of cellulose nanocrystal length and surface charge density through phosphoric acid hydrolysis. *Philosophical Transactions of the Royal Society A: Mathematical, Physical and Engineering Sciences* **376**, (2018).

53. Habibi, Y. *et al.* Bionanocomposites based on poly(ε-caprolactone)-grafted cellulose nanocrystals by ring-opening polymerization. *Journal of Materials Chemistry* **18**, 5002 (2008).

54. Khodayari, A., Hirn, U., Spirk, S., van Vuure, A. W. & Seveno, D. Recrystallization and size distribution of dislocated segments in cellulose microfibrils—a molecular dynamics perspective. *Cellulose* **28**, 6007–6022 (2021).

55. Spiliopoulos, P. *et al.* Visualizing degradation of cellulose nanofibers by acid hydrolysis. *Biomacromolecules* **22**, 1399–1405 (2021).

56. French, A. D. & Santiago Cintrón, M. Cellulose polymorphy, crystallite size, and the Segal Crystallinity Index. *Cellulose* **20**, 583–588 (2013).

57. Moroz, O. v. *et al.* The three-dimensional structure of the cellobiohydrolase Cel7A from Aspergillus fumigatus at 1.5 Å resolution. *Acta Crystallographica. Section F, Structural Biology Communications* **71**, 114 (2015).

58. Zaar, K. Visualization of pores (export sites) correlated with cellulose production in the envelope of the gram-negative bacterium Acetobacter xylinum. *Journal of Cell Biology* **80**, 773–777 (1979).

59. Du, J., Vepachedu, V., Cho, S. H., Kumar, M. & Nixon, B. T. Structure of the cellulose synthase complex of Gluconacetobacter hansenii at 23.4 Å resolution. *PLoS ONE* **11**, (2016).

60. Hu, S.-Q. *et al.* Structure of bacterial cellulose synthase subunit D octamer with four inner passageways. *Proceedings of the National Academy of Sciences* **107**, 17957–17961 (2010).

61. Zhao, Z. *et al.* Cellulose microfibril twist, mechanics, and implication for cellulose biosynthesis. *Journal of Physical Chemistry A* **117**, 2580–2589 (2013).

62. Cook, K. E. & Colvin, J. R. Evidence for a beneficial influence of cellulose production on growth of Acetobacter xylinum in liquid medium. *Current Microbiology: An International Journal* **3**, 203–205 (1980).

63. Mcqueen-Mason, S. & Cosgrove, D. J. Disruption of hydrogen bonding between plant cell wall polymers by proteins that induce wall extension. *Proc Natl Acad Sci U S A* **91**, 6574–6578 (1994).

64. Hayashi, T., Ogawa, K. & Mitsuishi, Y. Characterization of the adsorption of xyloglucan to cellulose. *Plant and Cell Physiology* **35**, 1199–1205 (1994).

65. Baba, K., Sone, Y., Misaki, A. & Hayashi, T. Localization of xyloglucan in the macromolecular complex composed of xloglucan and cellulose in pea stems. *Plant and Cell Physiology* **35**, 439–444 (1994).

66. Cosgrove, D. J. Growth of the plant cell wall. *Nature Reviews Molecular Cell Biology* **6**, 850–861 (2005).

67. Park, Y. W. *et al.* Enhancement of growth by expression of poplar cellulase in Arabidopsis thaliana. *Plant Journal* **33**, 1099–1106 (2003).

68. Moran-Mirabal, J. M. *et al.* Labeling and purification of cellulose-binding proteins for high resolution fluorescence applications. *Analytical Chemistry* **81**, 7981–7987 (2009).

69. Babi, M. *et al.* Efficient labeling of nanocellulose for high-resolution fluorescence microscopy applications. *Biomacromolecules* (2022) doi:10.1021/ACS.BIOMAC.1C01698.

70. Toyosaki, H. & Naritomi, T. Screening of bacterial cellulose-producing acetobacter strains suitable for agitated Culture. *Bioscience, Biotechnology, and Biochemistry* **59**, 1498–1502 (1995).

71. Ovesný, M., Křížek, P., Borkovec, J., Švindrych, Z. & Hagen, G. M. ThunderSTORM: A comprehensive ImageJ plug-in for PALM and STORM data analysis and super-resolution imaging. *Bioinformatics* **30**, 2389–2390 (2014).

72. Dong, X. M., Revol, J. F. & Gray, D. G. Effect of microcrystallite preparation conditions on the formation of colloid crystals of cellulose. *Cellulose* **5**, 19–32 (1998).

73. Briois, B. *et al.* Iα → Iβ transition of cellulose under ultrasonic radiation. *Cellulose* **20**, 597–603 (2013).